

Kinematics of gas and stars in the circumnuclear star-forming ring of NGC 3351

Guillermo F. Hägele,^{1★†} Ángeles I. Díaz,^{1‡} Mónica V. Cardaci,^{1,2†} Elena Terlevich^{3§} and Roberto Terlevich^{3§}

¹Departamento de Física Teórica, C-XI, Universidad Autónoma de Madrid, 28049 Madrid, Spain

²XMM Science Operations Centre, European Space Astronomy Centre of ESA, PO Box 50727, 28080 Madrid, Spain

³INAOE, Tonantzintla, Apdo. Postal 51, 72000 Puebla, México

Accepted 2007 March 19. Received 2007 March 7; in original form 2006 November 9

ABSTRACT

We have measured gas and stellar velocity dispersions in five circumnuclear star-forming regions (CNSFRs) and the nucleus of the barred spiral galaxy NGC 3351. The stellar dispersions have been obtained from high-resolution spectra of the Ca II triplet (CaT) lines at $\lambda\lambda 8494, 8542, 8662 \text{ \AA}$, while the gas velocity dispersions have been measured by Gaussian fits to the $H\beta$ $\lambda 4861 \text{ \AA}$ line on high-dispersion spectra.

The CNSFRs, with sizes of about 100 to 150 pc in diameter, are seen to be composed of several individual star clusters with sizes between 1.7 and 4.9 pc on a *Hubble Space Telescope* (HST) image. Using the stellar velocity dispersions, we have derived dynamical masses for the entire star-forming complexes and for the individual star clusters. Values of the stellar velocity dispersions are between 39 and 67 km s^{-1} . Dynamical masses for the whole CNSFRs are between 4.9×10^6 and $4.3 \times 10^7 M_{\odot}$ and between 1.8 and $8.7 \times 10^6 M_{\odot}$ for the individual star clusters.

Stellar and gas velocity dispersions are found to differ by about 20 km s^{-1} with the $H\beta$ lines being narrower than both the stellar lines and the [O III] $\lambda 5007 \text{ \AA}$ lines. We have found indications for the presence of two different kinematical components in the ionized gas of the regions. The radial velocity curve shows deviation from circular motions for the ionized hydrogen consistent with its infall towards the central regions of the galaxy at a velocity of about 25 km s^{-1} . To disentangle the origin of these two components it will be necessary to map these regions with high spectral and spatial resolution and much better signal-to-noise ratio in particular for the O^{2+} lines.

Key words: H II regions – galaxies: individual: NGC 3351 – galaxies: kinematics and dynamics – galaxies: starburst – galaxies: star clusters.

1 INTRODUCTION

The bulges of some nearby spiral galaxies show intense star-forming regions located in a roughly annular pattern around their nuclei. At optical wavelengths, these circumnuclear star-forming regions (CNSFRs) are easily observable rings. In the ultraviolet (UV), massive stars dominate the observed circumnuclear emission even in the presence of an active nucleus (González-Delgado et al. 1998; Colina et al. 2002). Cid Fernandes et al. (2001), for a representative

sample of 35 Seyfert 2 galaxies, find that about 40 per cent of them show unambiguous evidence of circumnuclear star formation within 300 pc of the nucleus and that these star-forming regions contribute about 30 to 50 per cent to the $H\beta$ total emission of the central zone.

These CNSFRs, with sizes going from a few tens to a few hundreds of parsec (e.g. Díaz et al. 2000), seem to be made of several H II regions ionized by luminous compact stellar clusters whose sizes, as measured from high spatial resolution *Hubble Space Telescope* (HST) images, are seen to be of only a few parsec. Their masses, as derived with the use of population synthesis models in circumnuclear regions of different galaxies, suggest that these clusters are gravitationally bound and that they might evolve into globular cluster configurations (Maoz et al. 1996). The luminosities of CNSFRs are rather large with absolute visual magnitudes (M_v) between -12 and -17 and $H\alpha$ luminosities between 2×10^{38}

*E-mail: guille.hagele@uam.es

†PhD fellow of Ministerio de Educación y Ciencia, Spain.

‡On sabbatical leave at IoA, Cambridge.

§Research affiliate at IoA.

and $7 \times 10^{40} \text{ erg s}^{-1}$. These values are comparable to those shown by 30 Dor, the largest H II region in the Large Magellanic Cloud (LMC), and overlap with those shown by H II galaxies (Melnick, Terlevich & Moles 1988; Díaz et al. 2000; Hoyos & Díaz 2006, and references therein).

Although these H II regions are very luminous not much is known about their kinematics or dynamics for both the ionized gas and the stars. It could be said that the worst known parameter of these ionizing clusters is their mass. There are different methods to estimate the mass of a stellar cluster. Classically one assumes that the system is virialized and determines the total mass inside a radius by applying the virial theorem to the observed velocity dispersion of the stars (σ_*). The stellar velocity dispersion is however hard to measure in young stellar clusters (a few million-years old) due to the shortage of prominent stellar absorption lines. The optical continuum between 3500 and 7000 Å shows very few lines since the light at these wavelengths is dominated by OB stars which have weak absorption lines at the same wavelengths of the nebular emission lines (Balmer H and He I lines). As pointed out by several authors (e.g. Ho & Filippenko 1996a), at longer wavelengths (8500 Å) the contamination due to nebular lines is much smaller and since red supergiant stars, if present, dominate the near-infrared (IR) light where the Ca II $\lambda\lambda 8498, 8542, 8662$ Å triplet (CaT) lines are found, these should be easily observable allowing the determination of σ_* (Terlevich et al. 1990; Prada, Greve & McKeith 1994). We have previously detected the CaT lines in CNSFRs but at a spectral resolution that was below that required to measure accurately their velocity dispersions (e.g. Terlevich et al. 1990).

Added interest in the study of CNSFRs comes from the fact that they are in general of high metal abundance (Díaz et al. 2006), therefore, they provide clues for the understanding of star formation phenomena at large metallicities, and, being close to the nuclear regions, for the determination of metallicity gradients in spiral galaxies.

NGC 3351 is an SBB(r)II spiral galaxy (Sandage & Tammann 1987) with coordinates $\alpha_{2000} = 10^{\text{h}}43^{\text{m}}57^{\text{s}}.7$, $\delta_{2000} = +11^{\circ}42'12''.7$. It was classified as a hotspot galaxy by Sérsic & Pastoriza (1967). Alloin & Nieto (1982) studied the star formation activity in the nuclear region and along a ring of about 20 arcsec in diameter using broad and narrow band images, concluding that NGC 3351 harbours high-mass star formation in these zones. In fact it can be considered a nuclear starburst galaxy since the star formation rate per unit area in the nuclear region, as estimated from the H α emission, compared to that in the disc is significantly increased (Devereux, Kenney & Young 1992). More recently, near-IR photometry in the *J* and *K* bands has been presented by Elmegreen et al. (1997) who derive a circumnuclear star formation rate of $0.38 \text{ M}_{\odot} \text{ yr}^{-1}$. From CO emission observations, Planesas, Colina & Pérez-Olea (1997) derive a mass of molecular gas of $3.5 \times 10^8 \text{ M}_{\odot}$.

*HST*UV images show that the present star formation in NGC 3351 is distributed along a nuclear ring with a major axis of 15 arcsec with star-forming regions arranged in complexes of diameters between 1.4 and 2.0 arcsec which are made up of several high surface brightness knots a few parsec in size embedded in a more diffuse component (Colina et al. 1997). No signs of activity have been observed in the nucleus of NGC 3351.

There are several values in the literature for the distance to NGC 3351. Here we adopt the distance derived by Graham et al. (1997) from Cepheid variable stars as part of the *HST* Key Project on the Extragalactic Distance Scale, which is 10.05 Mpc giving a linear scale of $\sim 49 \text{ pc arcsec}^{-1}$.

In this paper we present high-resolution far-red spectra ($\sim 0.39 \text{ Å pixel}^{-1} \sim 13.66 \text{ km s}^{-1} \text{ pixel}^{-1}$ at central wavelength,

$\lambda_c = 8563 \text{ Å}$) and stellar velocity dispersion measurements (σ_*) along the line-of-sight for the five CNSFRs and the nucleus of the spiral galaxy NGC 3351. We have also measured the ionized gas velocity dispersions (σ_g) from high-resolution blue spectra ($\sim 0.21 \text{ Å pixel}^{-1}$, $\sim 12.63 \text{ km s}^{-1} \text{ pixel}^{-1}$ at $\lambda_c = 4989 \text{ Å}$) using Balmer H β and [O III] emission lines. The comparison between σ_* and σ_g might throw some light on the yet unsolved issue about the validity of the gravitational hypothesis for the origin of the supersonic motions observed in the ionized gas in giant H II regions (Melnick, Tenorio-Tagle & Terlevich 1999).

Section 2 presents the details of the observations and the data reduction. Section 3 presents the results concerning the kinematics of gas and stars in each of the observed regions, as well as the determination of their masses. Section 4 is devoted to the discussion of these results, and finally the summary and conclusions of this work are presented in Section 5.

2 OBSERVATIONS AND DATA REDUCTION

2.1 Observations

High-resolution blue and far-red spectra were acquired as part of an observing run in 2000. They were obtained simultaneously using the blue and red arms of the Intermediate dispersion Spectrograph and Imaging System (ISIS) on the 4.2-m William Herschel Telescope (WHT) of the Isaac Newton Group (ING) at the Roque de los Muchachos Observatory on the Spanish island of La Palma. We used the EEV12 detector in the blue arm with a CCD binning factor of 2 both in 'x' and in 'y'. The H2400B grating was used to cover the wavelength range 4779–5199 Å ($\lambda_c = 4989 \text{ Å}$). The TEK4 CCD was attached to the red arm. In this case, the R1200R grating was used, covering a spectral range from 8363 to 8763 Å ($\lambda_c = 8563 \text{ Å}$). The spatial resolution of the observations was 0.2 and 0.36 arcsec pixel $^{-1}$ for the blue and red configurations, respectively. A slit width of 1 arcsec was used. The spectral ranges and grating resolutions [spectral dispersion in Å pixel $^{-1}$ and full width at half-maximum (FWHM) in Å measured on the sky lines] attained are given in Table 1 containing the journal of observations.

Three different slit positions were chosen to observe five CNSFRs and the nucleus of NGC 3351. In Fig. 1 we show the position of these slits at angles of 355°, 45° and 310° (which we have labelled S1, S2 and S3, respectively) overlapped on an image of the circumnuclear region of NGC 3351 acquired by the *HST* (see description below). The regions observed are identified on the H α map by Planesas et al. (1997) using their same nomenclature. The slit was positioned on the regions using the offsets from the nucleus, clearly visible during the data acquisition, given by Planesas et al. (1997).

Several bias and sky flat field frames were taken at the beginning and the end of each night in both arms. In addition, two lamp flat field and one calibration lamp exposure per each telescope position were performed. The calibration lamp used was CuNe+CuAr.

We have also downloaded two astrometrically and photometrically calibrated broad-band images of the central part of NGC 3351 from the Multimission Archive at Space Telescope.¹ The images were taken through the F606W (wide V) and the F160W (*H*) filters with the Wide Field and Planetary Camera 2 (WFPC2; PC1) and the Near-Infrared Camera and Multi-Object Spectrometer (NICMOS) Camera 3 both on-board the *HST*. They are displayed in Fig. 1, with the slit positions overlaid and the CNSFRs and the nucleus labelled.

¹ <http://archive.stsci.edu/hst/wfpc2>

Table 1. Journal of observations.

Date	Spectral range (Å)	Disp. (Å pixel ⁻¹)	FWHM (Å)	Spatial res. (arcsec pixel ⁻¹)	Position angle (°)	Exposure time (s)
2000 February 4	4779–5199	0.21	0.4	0.38	355	4 × 1200
2000 February 4	8363–8763	0.39	0.7	0.36	355	4 × 1200
2000 February 5	4779–5199	0.21	0.4	0.38	45	3 × 1200
2000 February 5	8363–8763	0.39	0.7	0.36	45	3 × 1200
2000 February 5	4779–5199	0.21	0.4	0.38	310	3 × 1200
2000 February 5	8363–8763	0.39	0.7	0.36	310	3 × 1200

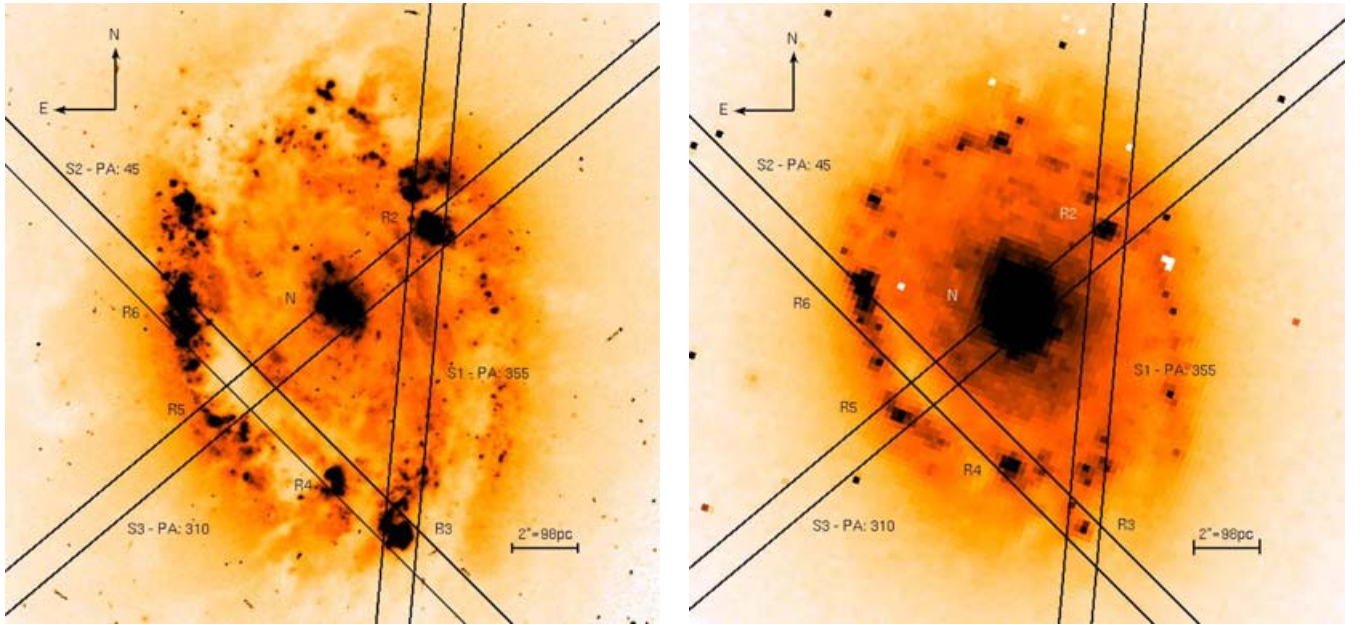


Figure 1. Left: F606W (wide V) image centred on NGC 3351 obtained with the WFC2 camera (PC1) of the *HST*. Right: *HST*-NICMOS image obtained through the F160W filter. For both images the orientation is north up, east to the left. The location and position angle of the WHT-ISIS slit positions, together with identifications of the CNSFRs extracted, are marked.

2.2 Data reduction

The data were processed and analysed using Image Reduction and Analysis Facility (IRAF)² routines in the usual manner. The procedure includes the removal of cosmic rays, bias subtraction, division by a normalized flat field and wavelength calibration. Wavelength fits were performed using 20–25 arc lines in the blue and 10–15 lines in the far-red by a polynomial of second to third order. These fits have been done at 50 and 60 locations along the slit in the blue and far-red, respectively, and they have yielded rms residuals between ~ 0.1 and ~ 0.2 pixel.

In the red, we also performed the wavelength calibration using sky lines following the work by Osterbrock et al. (1996). However, although more lines (20–25) were available for the calibration, the fits gave higher rms residuals, between ~ 0.3 and ~ 0.45 pixel since the low intensities of some of the lines did not allow a good Gaussian fit. We have therefore adopted the calibration made using only the arc lines.

² IRAF: the IRAF is distributed by the National Optical Astronomy Observatories, which is operated by the Association of Universities for Research in Astronomy, Inc. (AURA) under cooperative agreement with the National Science Foundation (NSF).

Background subtraction was performed using the spectra at both ends of the slit. This background includes light from the disc and bulge of the galaxy. It was almost impossible to neatly subtract the background bright emission lines in the far-red spectra due to the non-uniform and extended nebular emission surrounding each cluster and the variation over time of the sky emission lines. It is worth noting that these spurious features do not affect the CaT absorption lines.

We have not corrected the spectra for atmospheric extinction or performed any flux calibration, since our purpose was to measure radial velocities and velocity dispersions.

In addition to the galaxy frames, observations of 11 template velocity stars were made (four during the first night and seven during the second) to provide good stellar reference frames in the same system as the galaxy spectra for the kinematic analysis in the far-red. They are late-type giant and supergiant stars which have strong CaT features (see Díaz, Terlevich & Terlevich 1989). In Table 2 we list the spectral types and luminosity classes of the stars and the dates of observation.

Fig. 2 shows the spatial profiles of the $H\beta$ emission along each slit position. These $H\beta$ profiles have been generated by collapsing 11 pixels of the spectra in the direction of the resolution between 4860 and 4862 Å, rest-frame, $\lambda 4861$ being the centre of the $H\beta$ line, and are plotted as dashed lines. Continuum profiles were generated

Table 2. Stellar reference frames.

Star	ST-LC	Date
HD 71952	K0 I	2000 February 4
HD 129972	G6 I	
HD 134047	G6 III	
HD 144063	G4 III	
HD 16400	G5 III	2000 February 5
HD 22007	G5 I	
HD 22156	G6 III	
HD 92588	K1 I	
HD 102165	F7 I	
HD 115004	G8 III	
HD 116365	K3 III	

by collapsing 11 resolution pixels centred on 4844 \AA and are plotted as dash-dotted lines. The difference between the two is shown by solid lines and corresponds to the pure $H\beta$ emission. On these profiles we have selected the regions of the frames to be extracted in one-dimensional spectra corresponding to each of the identified CNSFRs. Those regions are marked by horizontal lines and labelled with their respective names in the figure. Spectra in slit positions 1 and 2 are placed along the circumnuclear ring and therefore any contribution from the underlying galaxy bulge is difficult to assess but the spatial profiles corresponding to slit position 3, that goes through the galactic nucleus, can be used to make an estimate. For the blue spectra the light from the underlying bulge is almost negligible amounting at most to 5 per cent at the $H\beta$ line. For the red spectra, the contribution is more important. From Gaussian fits to the $\lambda 8500 \text{ \AA}$ profile at slit position S3 we find that it amounts to about 20 per cent for the lowest surface brightness region, R5.

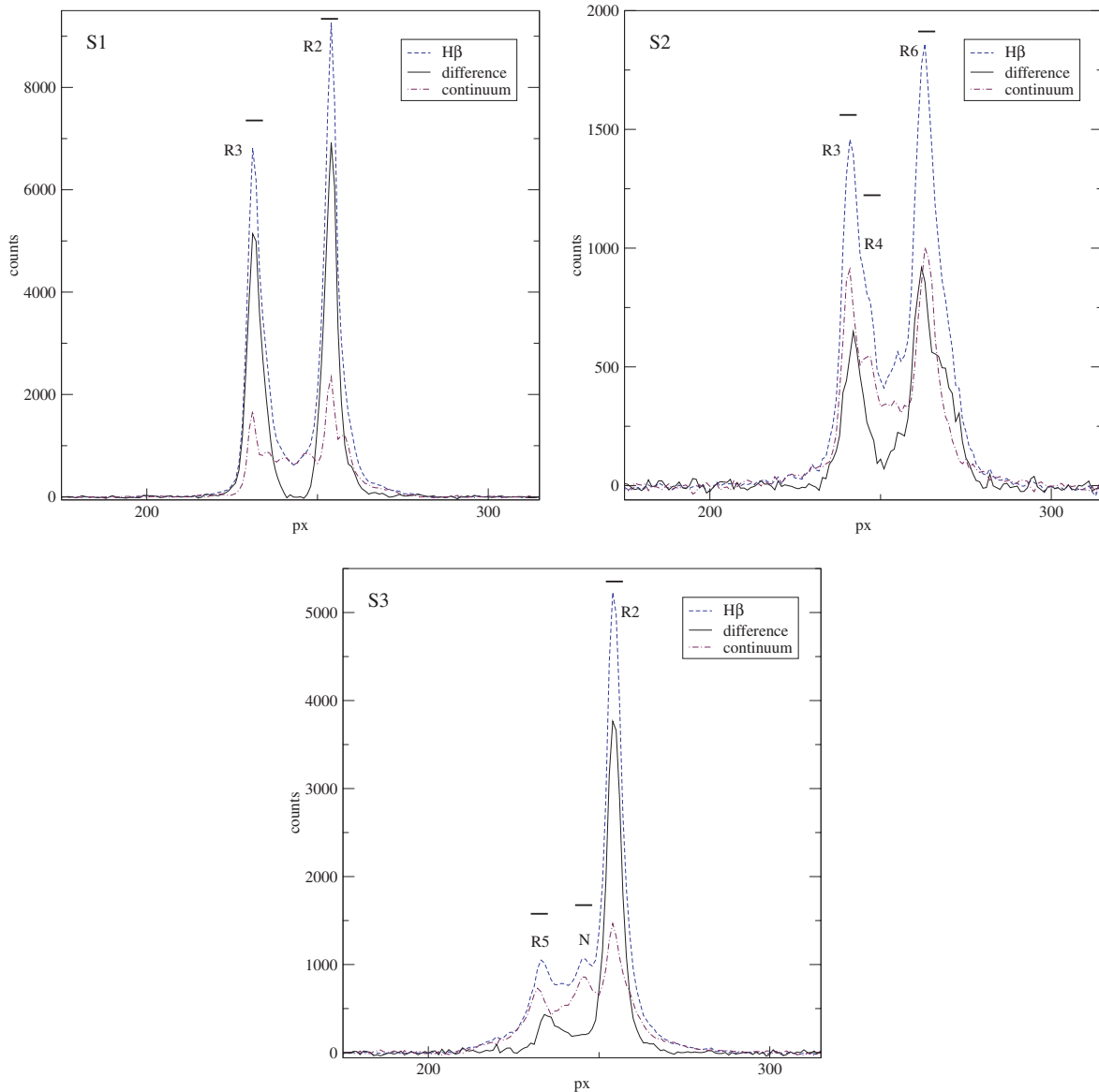


Figure 2. Spatial profiles of $H\beta$ for each slit corresponding to line+continuum (dashed line), continuum (dashed-dotted line) and the difference between them (solid line), representing the pure emission from $H\beta$. Pixel number increases to the north. Horizontal small lines show the location of the CNSFRs and nuclear apertures.

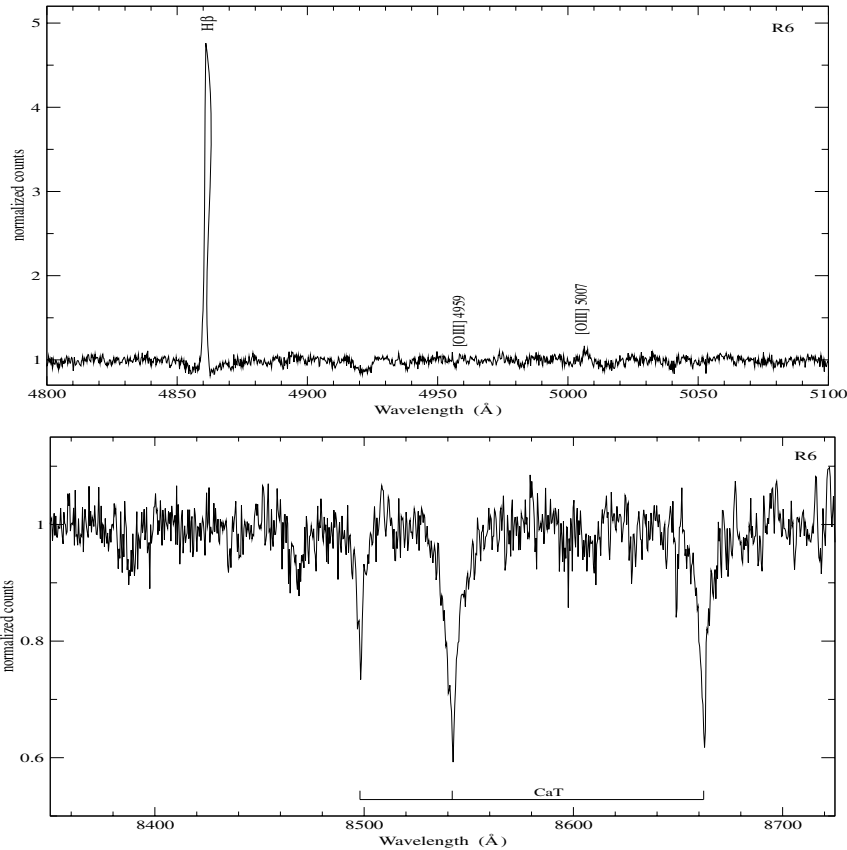


Figure 3. Blue (upper panel) and red (lower panel) rest-frame normalized spectra of R6. Notice the absence of conspicuous emission lines in the red spectral range for this region.

Similar values are found from inspection of the *HST*-NICMOS image shown in Fig. 1.

Figs 3 and 4 show representative spectra of these regions (R6 and R3, respectively) in the blue and the red spectral range split into two panels. The blue spectra show the Balmer $H\beta$ recombination line and the collisionally excited $[O\ III]$ lines at $\lambda\lambda 4959, 5007\ \text{\AA}$. Because of the high metallicity of the CNSFRs (Díaz et al. 2006), the lines of oxygen are seen to be very weak (see Fig. 5) and, in some cases, only the strongest $\lambda 5007\ \text{\AA}$ is detected (left-hand panel of this figure). The red spectra show the stellar CaT lines in absorption at $\lambda\lambda 8498, 8542, 8562\ \text{\AA}$. In some cases these lines are contaminated by Paschen emission (see for example the lower panel of Fig. 4) which occur at wavelengths very close to those of the CaT lines. In addition to these emission lines, it is possible to observe other emission features, such as $O\ I\ \lambda 8446$, $[Cl\ II]\lambda 8579$, Pa 14 and $[Fe\ II]\lambda 8617$. The observed red spectrum of R3 is plotted in Fig. 4 with a dashed line. A single Gaussian fit to the emission lines was performed and the lines were subsequently subtracted after checking that the theoretically expected ratio between the Paschen lines was satisfied. The solid line shows the subtracted spectrum.

3 RESULTS

3.1 Kinematics of stars and ionized gas

3.1.1 Stars

Stellar radial velocities and velocity dispersions were obtained from the absorption CaT lines using the cross-correlation tech-

nique described in detail by Tonry & Davis (1979). This method requires the comparison with a stellar template (which can be synthetic or observed) that represents the stellar population that best reproduces the conspicuous feature used to perform these measurements. An example of the red spectrum of a template star (HD 116365) is shown in Fig. 6 with the prominent features of CaT indicated. The line-of-sight velocity dispersions are calculated from the width of the primary peak of the cross-correlation function (CCF) after deconvolution of the instrumental profile. A filtering of high frequencies of the Fourier transform spectrum is usually included in this procedure to avoid noise contamination and a low frequency filtering is usually made to eliminate the residual continuum.

Minor changes/improvements with respect to the cross-correlation technique originally proposed by Tonry & Davis (1979) were introduced as described below. In order to apply this method, we have used XCSAO, an external package of IRAF within the RVSAO, which implements the cross-correlation method of Tonry and Davies and is a direct descendant of the system built by them (Kurtz & Mink 1998). We used late-type giant and supergiant stars that have strong CaT absorption lines (Fig. 6) as stellar velocity templates. We normalized the stellar spectra dividing by a fitted continuum and convolved each stellar spectrum template with a set of Gaussian functions of different σ simulating a wide range in velocity dispersions from 10 to 100 km s^{-1} with a bin size of 5 km s^{-1} . The obtained spectra are cross-correlated with the original template obtaining a relation between the width of the main peak of the cross-correlation and σ of the input Gaussian. This relation constitutes a correction curve for each template that is applied as described below to

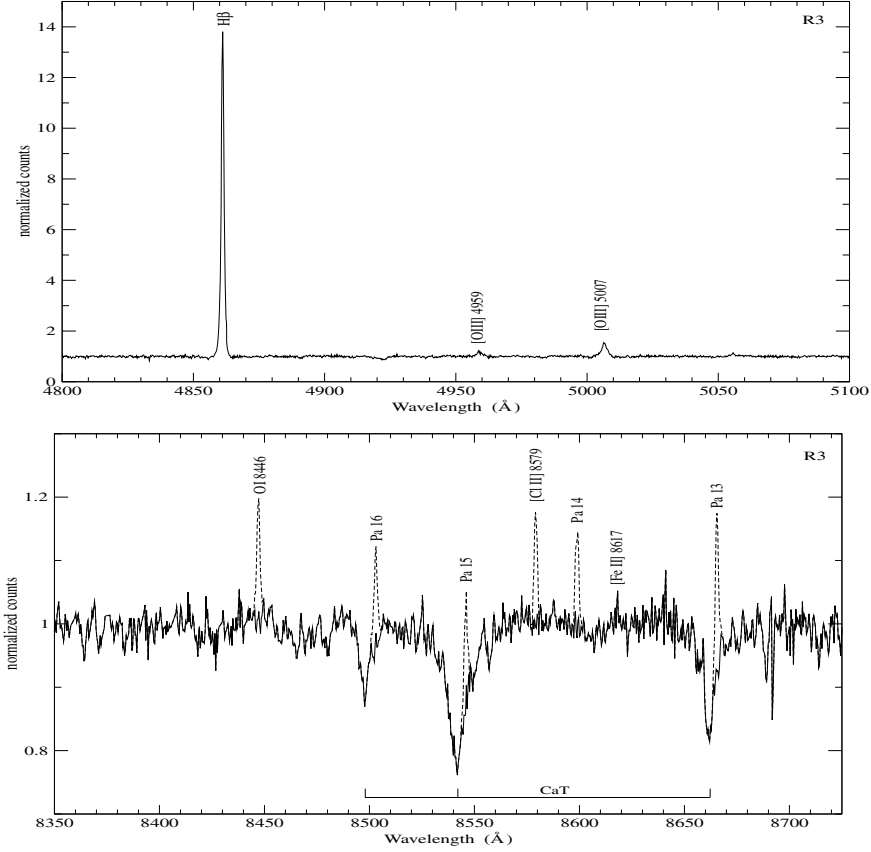


Figure 4. Blue (upper panel) and red (lower panel) rest-frame normalized spectra of R3. The dashed line in the lower panel shows the obtained spectrum; the solid line represents the spectrum after subtracting the emission lines (see text).

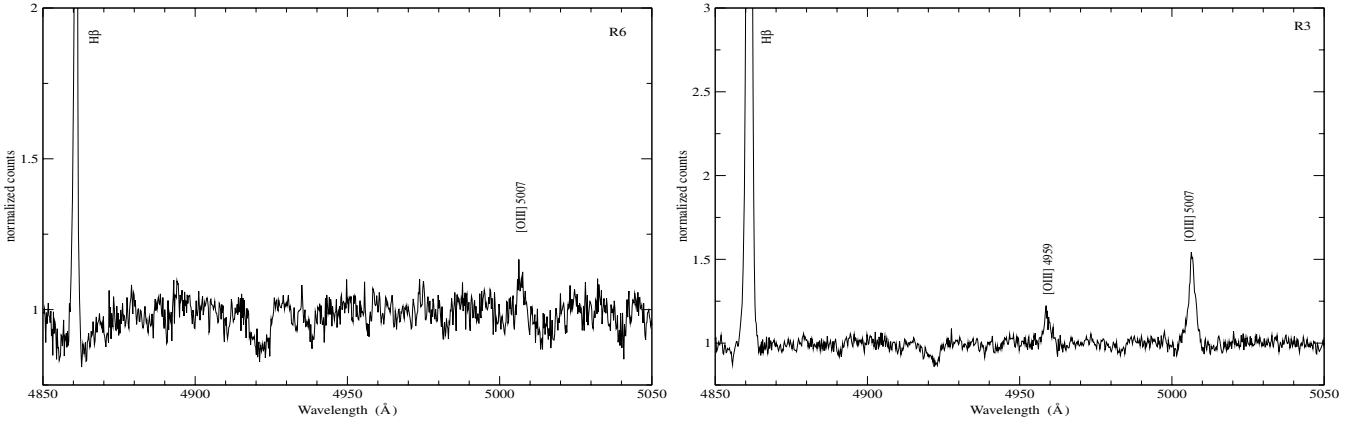


Figure 5. Enlargement of the blue rest-frame normalized spectra of R6 (left) and R3 (right).

obtain the stellar velocity dispersion for each CNSFR as described in Nelson & Whittle (1995). This procedure will allow us to correct for the known possible mismatches between template stars and the region composite spectrum. In Fig. 7 we show an example of these correction curves, in particular for HD 144063, together with a linear fit to it.

We determined the line-of-sight stellar velocity along each slit. Extractions were made every two pixels for slit position S1. For slit positions S2 and S3 they were made every three pixels, with one pixel overlap between consecutive extractions. In this way the signal-to-noise (S/N) ratio and the spatial resolution were optimized.

The stellar velocity dispersion was estimated at the position of each CNSFR and the nucleus using apertures of five pixels in all cases, which correspond to $1.0 \times 1.8 \text{ arcsec}^2$. A set of 11 templates of different spectral types and luminosity classes were used following Nelson & Whittle (1995) with the variation introduced by Palacios et al. (1997) of using the individual stellar templates instead of an average. To measure the velocity dispersion in a galactic spectrum we have convolved it with each stellar template, correcting the width of the main peak of the CCF (see Fig. 8) with the corresponding correction curve. Although the linear fits to the curves are very good approximations (see Fig. 7), we used a linear interpolation between

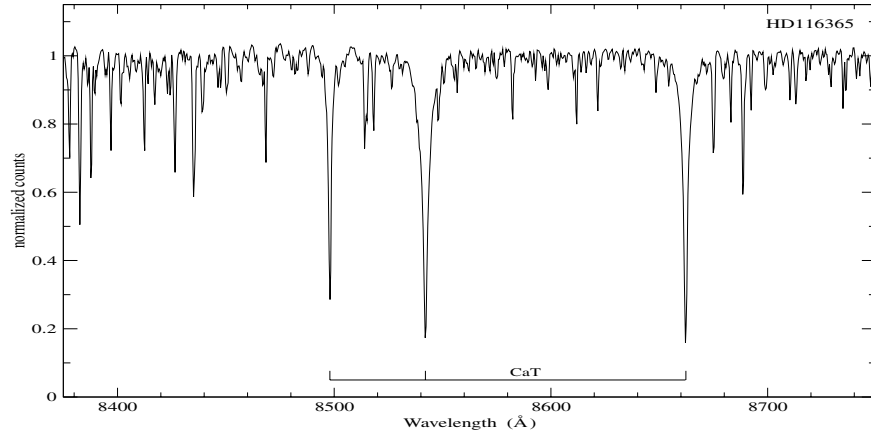


Figure 6. Red rest-frame normalized spectrum of HD 116365.

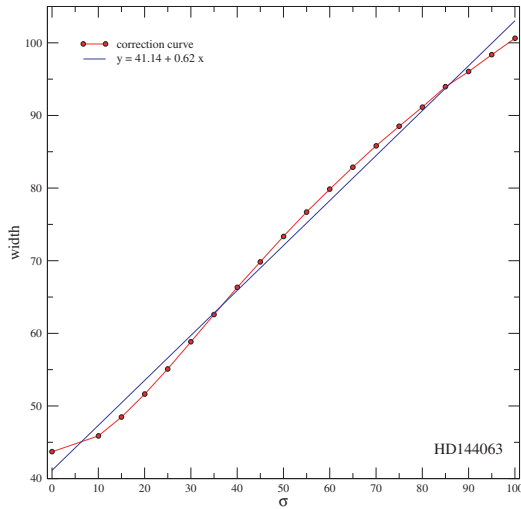


Figure 7. Velocity dispersions correction curve for HD 144063 (circles). The solid line is a linear fit to the curve.

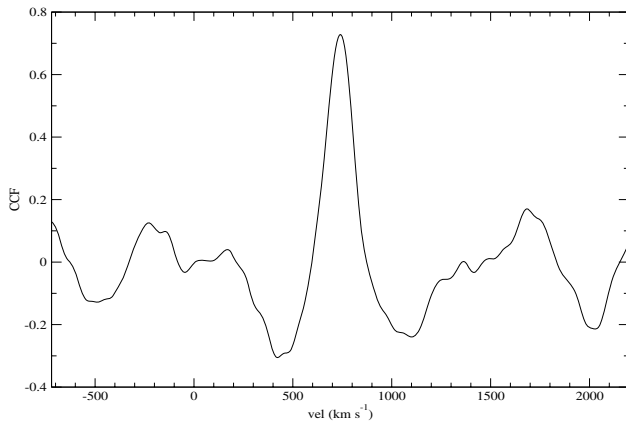


Figure 8. Example of the CCF.

the two nearest values to estimate the corrected width. The σ of the stars (σ_*) is the average of the σ values found for each stellar template and its error is given by the dispersion of the individual values of σ and the rms of the residuals of the wavelength fit. This

procedure allows a more accurate estimate of σ_* (Palacios et al. 1997). The radial velocities are the average of the radial velocities determined directly from the position of the main peak of the cross-correlation of each galaxy spectrum with each template in the rest-frame.

The stellar velocity dispersions are listed in column 3 of Table 3 along with their corresponding errors.

3.1.2 Ionized gas

The wavelength and the width of the $H\beta$ and $[O III]\lambda 5007 \text{ \AA}$ emission lines were measured to determine both the radial velocities and the velocity dispersions of the ionized gas. As in the case of the stars, we determined the radial velocity of the gas in the line-of-sight along each slit, every two pixels for S1 and every three pixels, superposing one pixel for consecutive extractions, for S2 and S3.

The velocity dispersion of the gas was estimated at the position of each CNSFR and the nucleus using five-pixel apertures, corresponding to $1.0 \times 1.9 \text{ arcsec}^2$. Following Jiménez-Benito et al. (2000) we adjusted three different suitable continua chosen by visual inspection and fitted a Gaussian to the whole line. Positions and widths of the emission lines are the average of the corresponding measurements and their errors are calculated as the dispersion of these measurements taking into account the rms of the residuals of the wavelength calibration. Thus, the error is associated with the continuum placement.

The velocity dispersions of the gas are calculated as

$$\sigma_{\text{gas}} = \sqrt{\sigma_m^2 - \sigma_i^2},$$

where σ_m and σ_i are the measured and instrumental dispersions, respectively. σ_i was measured directly from the sky emission lines and is about 10.5 km s^{-1} at $\lambda 4861 \text{ \AA}$.

Unexpectedly, the Gaussian fit just described revealed the presence of more than one component in the $H\beta$ lines. The optimal fit was found for two different components for all the regions. We then used the widths of those components to fit the $[O III]$ lines finding also optimal fits for regions R2 and R3 in the four analysed spectra corresponding to two different slit positions. For the rest of the regions the two-component fit did not show any improvement over the single component one, probably due to the low S/N ratio. An example of the fit for $H\beta$ and $[O III]\lambda 5007 \text{ \AA}$ can be seen in Fig. 9. The radial velocities found using this method are the same, within the errors, as those found by fitting a single component.

Table 3. Velocity dispersions.

Region	Slit	One component			Two components			
		σ_*	$\sigma_{\text{gas}}(\text{H}\alpha)$	$\beta_{\text{gas}}([\text{O III}])$	Narrow		Broad	
					$\sigma_{\text{gas}}(\text{H}\beta)$	$\sigma_{\text{gas}}([\text{O III}])$	$\sigma_{\text{gas}}(\text{H}\beta)$	$\sigma_{\text{gas}}([\text{O III}])$
R2	S1	50 ± 1	26 ± 1	72 ± 7	17 ± 3	21 ± 4	45 ± 3	74 ± 5
R2	S3	51 ± 6	29 ± 3	69 ± 9	16 ± 2	23 ± 5	43 ± 2	76 ± 8
R3	S1	55 ± 5	35 ± 1	67 ± 7	25 ± 3	28 ± 4	59 ± 4	71 ± 4
R3	S2	59 ± 7	39 ± 5	70 ± 7	24 ± 3	24 ± 6	59 ± 3	74 ± 9
R4	S2	66 ± 4	37 ± 4	76 ± 8	29 ± 3	–	65 ± 4	–
R5	S3	47 ± 4	34 ± 2	56 ± 7	30	–	76	–
R6	S2	39 ± 6	29 ± 6	46 ± 7	16 ± 3	–	46 ± 4	–
N	S3	67 ± 1	53 ± 3	73 ± 6	41 ± 5	–	67 ± 7	–

Note. Velocity dispersions in km s^{-1} .

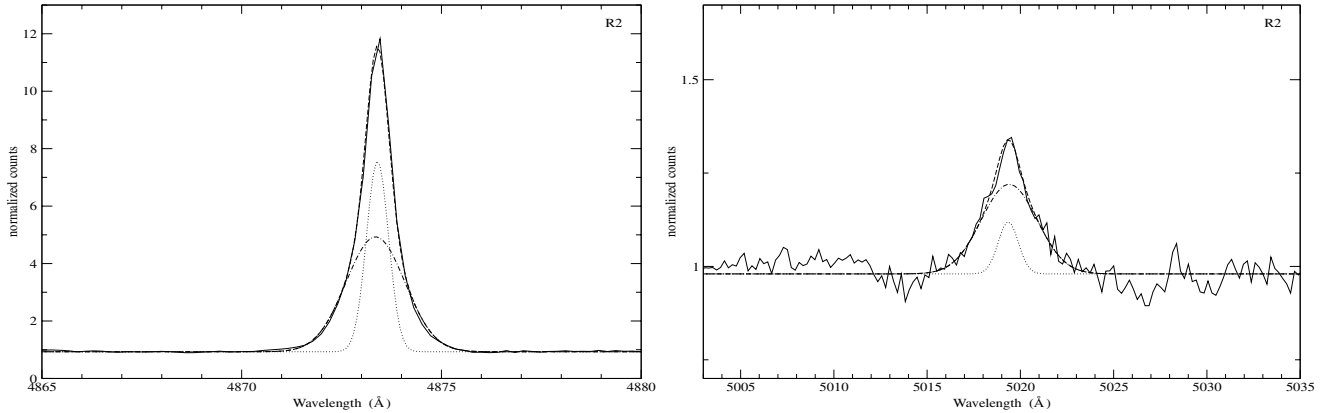


Figure 9. Sections of the normalized spectrum of R2. The left-hand panel shows from 4865 to 4880 Å containing H β and the right-hand panel shows from 5003 to 5035 Å containing the [O III] λ 5007 Å emission line. For both we have superposed the fits from the NGAUSSFIT task in IRAF; the dashed-dotted line is the broad component, the dotted line is the narrow component and the dashed line is the sum of both.

Gas velocity dispersions for H β and [O III] λ 5007 Å lines are given in Table 3. We have listed the velocity dispersions derived using the two different methods, the single line and the double line Gaussian fit. For the first method we have labelled the results as ‘One component’ (columns 4 and 5). For the second one, labels ‘Two components – Narrow’ (columns 6 and 7) and ‘Two components – Broad’ (columns 8 and 9) for the narrow and the broad component, respectively, are used.

3.2 Sizes

Two parameters are needed in order to determine the mass of a virialized stellar system, namely its velocity dispersion and its size. Previously estimated radii (R) for the regions, such as those given by Planesas et al. (1997) from H α images or given by Colina et al. (1997) from UV Space Telescope Imaging Spectrograph (STIS)-*HST* images, were defined to include the total integrated emission flux of the regions, and therefore they are not appropriate to calculate their dynamical masses, as what is needed for this is a measurement of the size of the mass distribution, i.e. the star-cluster size. This is traditionally done measuring the effective radius using images obtained in bands where the light is dominated by the stellar contribution and where the contamination by gaseous emission is either small or can be estimated and corrected.

Following Ho & Filippenko (1996a) we have defined the radius (R) of a given structure as in Meurer et al. (1995) assuming that they have an intrinsically circularly symmetric Gaussian profile. As we can see in Fig. 10 this is a rather good approximation.

We have determined the FWHM, W_{50} , by superposing the contours in the F606W WFPC2-*HST* image and determining the half light strength between the peak of the intensity for each region and the galaxy background (red contours in the electronic version of the paper). Then, for this model, we take R as the half light radius, $R = 0.5 \times W_{50}$. While Meurer et al. (1995) measured the sizes from an H α image, we only have the F606W (wide V; containing H α) image in this spectral range and with the appropriate spatial resolution.

We find, as expected, that several of these regions are composed of more than one knot. Only R4 and R5 seem to have a unique principal knot, at least at the PC1 spatial resolution. In the most extreme case, R6, we find at least 18 knots with a detection level of 10σ above background level. All these knots are within the radius of the regions defined by Planesas et al. (1997). We have to remark that our search for knots has not been exhaustive since that is not the aim of this work. The radii of the single knots vary between 1.7 and 4.9 pc.

Position, radius and its error and the peak intensity in counts measured from the WFPC2 image are listed in Table 4 for each knot identified.

3.3 Masses

3.3.1 Dynamical masses

We have used the virial theorem to estimate upper limits to the dynamical masses (M_*) inside the half light radius (R) for each observed knot in the F606W WFPC2-*HST* image. In order to do

Table 4. Positions, radii and peak intensities.

Region	Position		R (pc)	I (counts)
	$\alpha_{J2000.0}$	$\delta_{J2000.0}$		
R2	10 ^h 43 ^m 57 ^s .12	+11°42′08″.27	4.9 ± 0.2	2531
R2a	10 ^h 43 ^m 57 ^s .12	+11°42′08″.53	2.5 ± 0.2	956
R3	10 ^h 43 ^m 57 ^s .16	+11°41′59″.02	3.9 ± 0.2	2598
R3a	10 ^h 43 ^m 57 ^s .16	+11°41′59″.24	2.2 ± 0.1	1852
R3b	10 ^h 43 ^m 57 ^s .18	+11°41′58″.93	2.0 ± 0.3	1032
R3c	10 ^h 43 ^m 57 ^s .21	+11°41′59″.41	2.5 ± 0.3	546
R3d	10 ^h 43 ^m 57 ^s .21	+11°41′59″.33	2.7 ± 0.3	489
R3e	10 ^h 43 ^m 57 ^s .20	+11°41′59″.71	2.9 ± 0.2	383
R3f	10 ^h 43 ^m 57 ^s .20	+11°41′59″.26	3.7 ± 0.4	330
R4	10 ^h 43 ^m 57 ^s .32	+11°42′00″.92	2.9 ± 0.1	2581
R5	10 ^h 43 ^m 57 ^s .55	+11°42′02″.50	3.2 ± 0.1	973
R6	10 ^h 43 ^m 57 ^s .60	+11°42′05″.21	2.7 ± 0.1	2399
R6a	10 ^h 43 ^m 57 ^s .62	+11°42′06″.81	2.0 ± 0.1	794
R6b	10 ^h 43 ^m 57 ^s .62	+11°42′06″.00	2.0 ± 0.2	714
R6c	10 ^h 43 ^m 57 ^s .63	+11°42′06″.38	2.0 ± 0.1	551
R6d	10 ^h 43 ^m 57 ^s .62	+11°42′05″.86	1.7 ± 0.1	404
R6e	10 ^h 43 ^m 57 ^s .65	+11°42′06″.85	2.4 ± 0.2	376
R6f	10 ^h 43 ^m 57 ^s .62	+11°42′06″.21	2.0 ± 0.1	340
R6g	10 ^h 43 ^m 57 ^s .61	+11°42′06″.12	1.7 ± 0.1	295
R6h	10 ^h 43 ^m 57 ^s .63	+11°42′06″.52	1.7 ± 0.1	290
R6i	10 ^h 43 ^m 57 ^s .64	+11°42′06″.13	2.0 ± 0.1	285
R6j	10 ^h 43 ^m 57 ^s .62	+11°42′05″.66	2.9 ± 0.3	282
R6k	10 ^h 43 ^m 57 ^s .61	+11°42′05″.41	2.4 ± 0.2	275
R6l	10 ^h 43 ^m 57 ^s .61	+11°42′06″.31	2.4 ± 0.3	272
R6m	10 ^h 43 ^m 57 ^s .61	+11°42′05″.43	2.2 ± 0.2	270
R6n	10 ^h 43 ^m 57 ^s .63	+11°42′05″.52	2.2 ± 0.3	251
R6o	10 ^h 43 ^m 57 ^s .63	+11°42′04″.83	2.9 ± 0.3	212
R6p	10 ^h 43 ^m 57 ^s .61	+11°42′04″.81	3.1 ± 0.3	212
R6q	10 ^h 43 ^m 57 ^s .56	+11°42′05″.48	2.2 ± 0.3	211
N	10 ^h 43 ^m 57 ^s .29	+11°42′05″.81	11.3 ± 0.1	513

this, we have assumed that the systems are spherically symmetric, gravitationally bound and have isotropic velocity distribution [$\sigma^2(\text{total}) = 3\sigma_*^2$]. Then, the dynamical mass is given by $M_* = 3\sigma_*^2 R/G$ (Ho & Filippenko 1996a,b).

It must be noted that we have measurements for the size of each knot (typically 5 pc), but we do not have direct access to the stellar velocity dispersion of each of the clusters, since our spectroscopic measurements encompass a wider area ($1.0 \times 1.8 \text{ arcsec}^2 \sim 49 \times 88 \text{ pc}^2$) that includes the CNSFRs to which each group of knots belong. The use of these wider size scale velocity dispersion measurements to estimate the mass of each knot, lead us to overestimate the mass of the individual clusters, and hence of each CNSFR.

However, as can be seen in the *HST*-NICMOS image (right-hand panel of Fig. 1), the CNSFRs of NGC 3351 are clearly visible in the IR and dominate the light inside the apertures observed. All the regions analysed show up very prominently in the near-IR and therefore we can assume that the light at the CaT wavelength region is dominated by the stars in the clusters. The IR CaT is very strong, in fact the strongest stellar feature, in very young clusters, i.e. older than 4 Myr (Terlevich et al. 1990). Besides, we detect a minimum in the velocity dispersion at the position of the clusters, indicating that they are kinematically distinct. We cannot be sure though that we are actually measuring their velocity dispersion and thus prefer to say that our measurements of σ_* and hence dynamical masses constitute upper limits. Although we are well aware of the difficulties, still we are confident that these upper limits are valid and important for comparison with the gas kinematical measurements.

Table 5. Dynamical masses.

Region	Slit	M_*	Error (per cent)
R2	S1	85 ± 5	
R2a	S1	44 ± 4	
R2sum	S1	129 ± 6	3.4
R2	S3	87 ± 21	
R2a	S3	44 ± 11	
R2sum	S3	131 ± 23	17.8
R2 (adopted)		129 ± 6	3.4
R3	S1	82 ± 14	
R3a	S1	46 ± 8	
R3b	S1	42 ± 9	
R3c	S1	52 ± 11	
R3d	S1	57 ± 11	
R3e	S1	61 ± 11	
R3f	S1	78 ± 15	
R3sum	S1	417 ± 31	7.3
R3	S2	94 ± 23	
R3a	S2	53 ± 13	
R3b	S2	48 ± 14	
R3c	S2	60 ± 16	
R3d	S2	65 ± 17	
R3e	S2	70 ± 17	
R3f	S2	89 ± 5	
R3sum	S2	477 ± 47	9.9
R3 (adopted)		447 ± 56	12.6
R4	S2	87 ± 12	13.9
R5	S3	49 ± 8	16.4
R6	S2	29 ± 9	
R6a	S2	21 ± 8	
R6b	S2	21 ± 8	
R6c	S2	21 ± 8	
R6d	S2	18 ± 7	
R6e	S2	26 ± 10	
R6f	S2	21 ± 8	
R6g	S2	18 ± 7	
R6h	S2	18 ± 7	
R6i	S2	21 ± 8	
R6j	S2	31 ± 12	
R6k	S2	26 ± 10	
R6l	S2	26 ± 10	
R6m	S2	24 ± 9	
R6n	S2	24 ± 9	
R6o	S2	31 ± 12	
R6p	S2	33 ± 13	
R6q	S2	24 ± 9	
R6sum	S2	434 ± 39	9.0
N	S3	350 ± 11	3.1

Note. Masses in $10^5 M_\odot$.

The estimated dynamical masses and their corresponding errors for each knot are listed in Table 5. For the regions that have been observed in more than one slit position, we list the derived values using the two different stellar velocity dispersions. The dynamical masses in the lines labelled ‘sum’ are the sum of the values derived for each knot of the corresponding region, when there are more than one. The ‘adopted’ dynamical mass for R2 is directly the sum of the dynamical masses of the two knots derived using the velocity dispersion estimated from S1 since the mass calculated from S3

is in agreement with the first one (see Table 5) but it has a much greater error. This greater error is due to the lower S/N ratio of the spectrum of R2 extracted from S3. In contrast, the derived dynamical masses for R3 are not in complete agreement, although they coincide within the errors, which are comparable. In this case we have taken the average as the ‘adopted’ value. The fractional error in the ‘sum’ and the adopted values of the dynamical masses of the CNSFRs are listed in column 4 of Table 5.

3.3.2 Ionizing star clusters

We have derived the masses of the ionizing star clusters (M_{ion}) from the total number of ionizing photons using solar metallicity single burst models by García-Vargas, Bressan & Díaz (1995), assuming a Salpeter initial mass function (Salpeter 1955; IMF) with lower and upper mass limits of 0.8 and $120 M_{\odot}$ which provide the number of ionizing photons per unit mass, $Q(H_0)/M_{\text{ion}}$. This number decreases with the age of the region. We have used the following relation between $Q(H_0)/M_{\text{ion}}$ and the equivalent width (EW) of $H\beta$, $\text{EW}(H\beta)$, derived from the models, in order to take into account the evolutionary state of the region (Díaz 1998):

$$\log(Q(H_0)/M_{\text{ion}}) = 44.48 + 0.86 \log(\text{EW}(H\beta)).$$

We have taken the values of $\text{EW}(H\beta)$ from Pérez-Olea (1996) (see Table 6) which are not corrected by the contribution to the continuum by the underlying stellar population. This correction would increase the values of $\text{EW}(H\beta)$ thus decreasing the calculated M_{ion} . The total number of ionizing photons has been derived from the $H\alpha$ luminosities (Leitherer & Heckman 1995):

$$Q(H_0) = 7.35 \times 10^{11} L(H\alpha).$$

We have taken the total observed $H\alpha$ luminosities from Planesas et al. (1997) correcting them for the different assumed distance. These authors estimated a diameter of 2.4 arcsec for each whole region and the nucleus, except for R4 for which they used 2.2 arcsec. We have corrected the $H\alpha$ luminosities for internal extinction using the colour excess $[E(B - V)]$ estimated by Pérez-Olea (1996) and assuming the galactic extinction law of Miller & Mathews (1972) with $R_v = 3.2$.

Our derived values of $Q(H_0)$ are lower limits since we have not taken into account either the absorption of photons by dust or any photon escape from the $H\text{II}$ regions.

The final expression for the derivation of M_{ion} is

$$M_{\text{ion}} = \frac{7.35 \times 10^{11} L(H\alpha)}{10^{44.48+0.86 \log[\text{EW}(H\beta)]}}.$$

3.3.3 Ionized gas

The amount of ionized gas (M_{HII}) associated to each star-forming region complex has been obtained from our derived $H\alpha$ luminosities using the relation given by Macchetto et al. (1990) for an electron temperature of 10^4 K:

$$M_{\text{HII}} = 3.32 \times 10^{-33} L(H\alpha) N_e^{-1},$$

where N_e is the electron density. The electron density for each region (obtained from the $[\text{SII}]\lambda\lambda 6717/6731$ Å line ratio) has been taken from Díaz et al. (2006) for the CNSFRs and from Pérez-Olea (1996) for the nucleus (see Table 6).

In Table 6 we have listed for each region and the nucleus, the $H\alpha$ luminosities $[L(H\alpha)]$ (corrected and uncorrected for reddening), the colour excess, $E(B - V)$, the logarithmic extinction at $H\alpha$, $C(H\alpha)$, the number of ionizing photons, $Q(H_0)$, the EW of $H\beta$, $\text{EW}(H\beta)$, the electron density, N_e , and the masses of the ionizing stellar cluster, M_{ion} , and of the ionized hydrogen, M_{HII} .

3.4 Emission line ratios

We have used two different ways to integrate the intensity of a given line: (1) in the cases of a single Gaussian fit the emission line intensities were measured using the *SPLIT* task of *IRAF*. The positions of the local continua are placed by eye. For the $H\beta$ emission lines a conspicuous underlying stellar population is easily appreciable by the presence of absorption features that depress the lines (see discussion in Díaz 1988). Examples of this effect can be appreciated in Fig. 5. We have then defined a pseudo-continuum at the base of the line to measure the line intensities and minimize the errors introduced by the underlying population (for details see Hägele et al. 2006). (2) In the cases of a fit by two Gaussians the individual intensities of the narrow and broad components are estimated from the fitting parameters using the expression $I = 1.0645 A \text{FWHM}$ ($= \sqrt{2\pi} A \sigma$), where I is the Gaussian intensity, A is the amplitude of the Gaussian and FWHM is the full width at half-maximum (σ is the dispersion of the Gaussian). A pseudo-continuum for the $H\beta$ emission line was also defined in these cases.

Following González-Delgado et al. (1994), Castellanos, Díaz & Terlevich (2002) and Pérez-Montero & Díaz (2003), the statistical errors associated with the observed emission fluxes have been calculated using the expression $\sigma_1 = \sigma_c N^{1/2} [1 + \text{EW}/(N\Delta)]^{1/2}$, where σ_1 is the error in the observed line flux, σ_c represents the standard deviation in a box near the measured emission line and stands for the error in the continuum placement, N is the number of pixels used in the measurement of the line intensity, EW is the line equivalent

Table 6. Physical parameters.

Region	$L_{\text{obs}}(H\alpha)^a$	$E(B - V)^b$	$C(H\alpha)$	$L(H\alpha)$	$Q(H_0)$	$\text{EW}(H\beta)^b$	M_{ion}	N_e^c	M_{HII}	M_{ion}/M_* (per cent)
R2	19.3	0.17	0.02	20.5	15.0	9.5	7.2	440	0.15	5.6
R3	25.0	0.46	0.65	111.0	81.5	16.5	24.2	430	0.86	5.4
R4	12.7	0.27	0.24	22.0	16.2	13.0	5.9	310	0.24	6.8
R5	5.9	0.25	0.20	9.2	6.8	5.1	5.5	360	0.09	11.3
R6	7.5	0.0	-0.34	3.4	2.5	2.3	4.1	360	0.03	1.0
N	3.3	0.07	-0.19	2.1	1.6	1.8	3.1	650 \ddagger	0.01	0.9

Note. Luminosities in $10^{38} \text{ erg s}^{-1}$, masses in $10^5 M_{\odot}$, ionizing photons in $10^{50} \text{ photon s}^{-1}$ and densities in cm^{-3} .

^aFrom Planesas et al. (1997) corrected for the different adopted distances.

^bFrom Pérez-Olea (1996).

^cFrom Díaz et al. (2006).

Table 7. Line ratios.

Region	Slit	One component	Two components		$\log([\text{N II}]\lambda 6584/\text{H}\beta)^a$
		$\log([\text{O III}]\lambda 5007/\text{H}\beta)$	Narrow $\log([\text{O III}]\lambda 5007/\text{H}\beta)$	Broad $\log([\text{O III}]\lambda 5007/\text{H}\beta)$	
R2	S1	-1.07 ± 0.06	-1.66 ± 0.08	-0.93 ± 0.12	-0.43 ± 0.01
R2	S3	-1.01 ± 0.06	-1.55 ± 0.08	-0.96 ± 0.13	
R3	S1	-1.10 ± 0.06	-1.57 ± 0.07	-0.93 ± 0.10	-0.42 ± 0.01
R3	S2	-1.00 ± 0.06	-1.52 ± 0.09	-0.89 ± 0.10	
R4	S2	-1.03 ± 0.07	–	–	-0.49 ± 0.01
R5	S3	-0.85 ± 0.12	–	–	-0.37 ± 0.03
R6	S2	-1.09 ± 0.11	–	–	-0.52 ± 0.02
N	S3	-0.28 ± 0.05	–	–	

^aFrom Díaz et al. (2006).

width and Δ is the wavelength dispersion in \AA pixel^{-1} . For the $\text{H}\beta$ emission line we have doubled the derived error, σ_1 , in order to take into account the uncertainties introduced by the presence of the underlying stellar population (Hägele et al. 2006).

The logarithmic ratio between the emission line intensities of $[\text{O III}]\lambda 5007 \text{ \AA}$ and $\text{H}\beta$, and their corresponding errors, are presented in Table 7. We have also listed in this table the logarithmic ratio between the emission line fluxes of $[\text{N II}]\lambda 6584 \text{ \AA}$ and $\text{H}\alpha$ together with their corresponding errors from Díaz et al. (2006).

4 DISCUSSION

The upper panel of Fig. 11 shows the relation between the velocity dispersions of gas and stars. Circles correspond to gas velocity dispersions measured from the $\text{H}\beta$ emission line using a single Gaussian fit. Squares and triangles correspond to measurements performed using two-component Gaussian fits, squares for the broad component and triangles for the narrow one. The straight line shows the one-to-one relation. As a general result, the $\text{H}\beta$ velocity dispersions derived by a single Gaussian fit are lower than the stellar ones by about 25 km s^{-1} . This is also the case for the Paschen lines in the two regions where they could be measured. On the other hand, a good agreement is found between the stellar velocity dispersions and those of the broad component of $\text{H}\beta$. The deviant point, marked with arrows, corresponds to the region with the lowest S/N ratio (R5) for which the fits do not provide accurate results. The narrow component shows velocity dispersions even lower than those obtained by single Gaussian fits. The ratio between the fluxes in the narrow and broad components is between 0.7 and 0.95 (except for the case of R5 for which no meaningful result is found).

The lower panel of Fig. 11 shows the relation between the stellar velocity dispersions and those of the $[\text{O III}]$ emission line measured by both single- and two-component Gaussian fits, which due to the weakness of the line (see Figs 3 to 5), could be done in only four cases, corresponding to the two slit positions on regions R2 and R3. In this case, the broad component seems to dominate the width of the emission line which again agrees with the stellar one. The width of the narrow component, in the cases in which the two-component fit was possible, is comparable to that of the narrow component of the $\text{H}\beta$ line.

The two gaseous components have been plotted separately in Fig. 12 which shows their location in the $[\text{O III}]/\text{H}\beta$ versus $[\text{N II}]/\text{H}\alpha$ diagram (Baldwin, Phillips & Terlevich 1981) together with a sample of emission line galaxies (including H II -like objects) from the Sloan Digital Sky Survey – Data Release 3 (SDSS-DR3) (López 2005) and H II regions from the sample of Pérez-Montero & Díaz

(2005). The two systems are clearly segregated in this diagnostic diagram with the narrow component showing the lowest excitation of the two and occupying the same position in the diagram as the starburst systems in the SDSS data set with the lowest excitation found.

Fig. 13 shows the radial velocities along the slit for each slit position as derived from the ionized gas emission lines and stellar absorptions. The turnover points of the rotational curves seem to be located at the same position than the star-forming ring, specially for the S3 slit position that crosses the centre of the galaxy, as found in other galaxies (see Telesco & Decher 1988; Díaz et al. 1999, and references therein). For the systemic velocity of NGC 3351, the derived values are consistent with those previously obtained by Rubin, Peterson & Ford (1975) and Planesas et al. (1997), and with the velocity distribution expected for this type of galaxies (Binney & Tremaine 1987).

The rotation velocities derived for both stars and gas are in reasonable agreement, although in some cases the gas seems to rotate somewhat faster than the stars. In fact, in the lower panel of Fig 13, which corresponds to the slit position passing through the nucleus, it is interesting to note that at the maximum and minimum of the velocity curve, which correspond approximately to the positions of regions R5 and R2, the $\text{H}\beta$ emission line shows velocities lower and higher than the stars by about 25 and 30 km s^{-1} , respectively. This could be interpreted as motions of the ionized hydrogen deviating from rotation and consistent with a radial infall to the central regions of the galaxy. A similar result was found by Rubin et al. (1975) from high dispersion observations of the $\text{H}\alpha$ line in the central region of this galaxy. Their preferred model for the fitting of the kinematical data consists of gas which is rotating and contracting with $V_{\text{rot}} = 126 \pm 16 \text{ km s}^{-1}$ and $V_{\text{cont}} = 34 \pm 11 \text{ km s}^{-1}$.

It is clearly of major interest to find out how widespread is the presence of two distinct components in the emission lines in ionized regions and what is its influence on the observed line ratios for several reasons. First, a change in position in the diagnostic diagrams would certainly affect the classification of the activity in the central regions of the concerned galaxies. Secondly, it will affect the inferences about the nature of the source of ionization in the two components. Thirdly, it could have an influence on the gas abundance determinations given that the ratio of the narrow to the broad components of $\text{H}\beta$ is about 1. Clearly, it is not possible to use global line ratios to estimate gaseous abundances if the permitted and forbidden line fluxes are partially originated in different kinematical systems. To disentangle the origin of these two components it will be necessary to map these regions with high spectral and spatial resolution and much better S/N ratio in particular for the

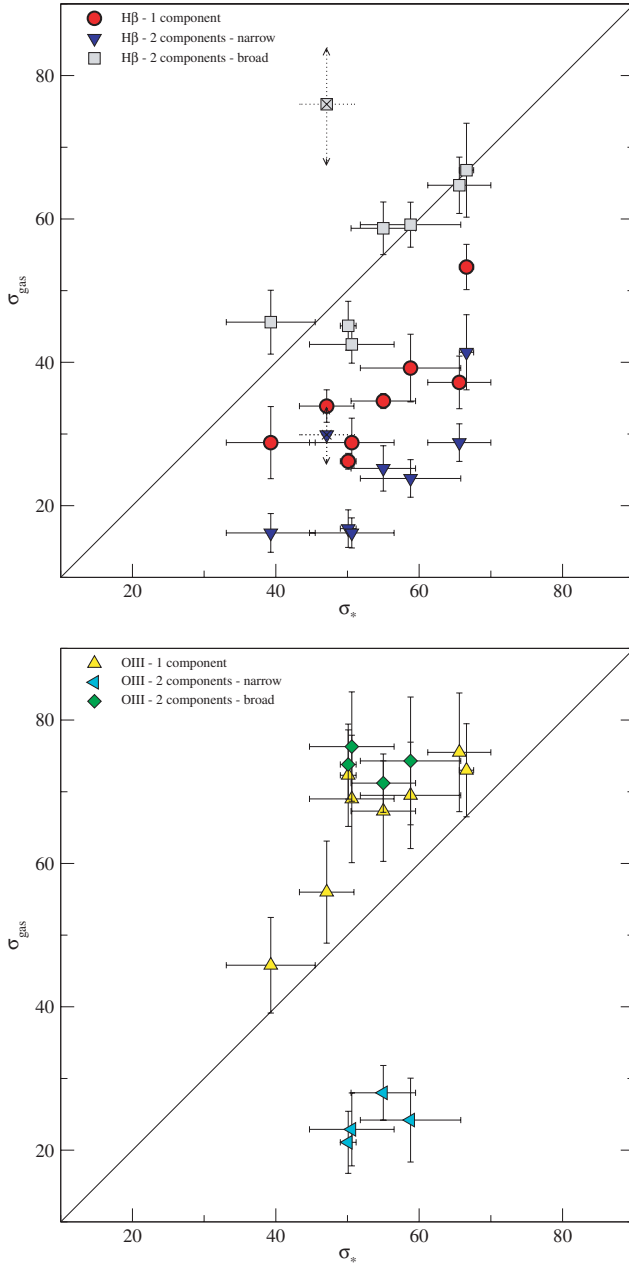


Figure 11. Upper panel: relation between velocity dispersions of the gas (derived from $H\beta$) and stars (CaT) for the CNSFRs and the nucleus. Symbols are as follows: single Gaussian fit, circles; two Gaussian fit, broad component, squares; narrow component, triangles. Lower panel: as the upper panel for the $[O III]$ line. Upward triangles correspond to the estimates using a single Gaussian fit, diamonds represent the broad components of the two Gaussian fit and left triangles, the narrow components.

O^{2+} lines. Three-dimensional (3D) spectroscopy with Integral Field Units (IFUs) would be the ideal tool to approach this issue.

Our values of the dynamical masses have been derived from stellar velocity dispersion measurements as mapped by the CaT absorption lines and the sizes measured on an *HST* image. They are in the range between 4.9×10^6 and $4.3 \times 10^7 M_{\odot}$ for the CNSFRs and is $3.5 \times 10^7 M_{\odot}$ for the nuclear region inside the inner 11.3 pc (see Table 5). The fractional errors of the dynamical masses of the CNSFRs are between ~ 3.4 and ~ 17.8 per cent, and is ~ 3.1 per cent

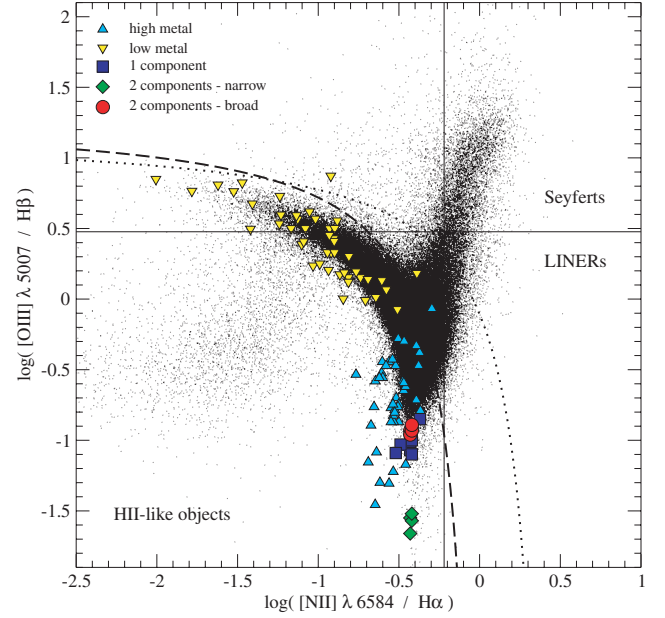


Figure 12. BPT (Baldwin, Phillips and Terlevich) diagram $[O III]/H\beta$ versus $[N II]/H\alpha$. Squares correspond to the ratio of the emission intensities of $[O III]$ and $H\beta$ estimated using a single Gaussian fit, diamonds to the narrow components of the two Gaussian fits and circles to the broad components. Dotted and dashed curves are the boundary between active galactic nuclei (AGNs) and $H II$ galaxies defined by Kewley et al. (2001) and Kauffmann et al. (2003), respectively. The solid horizontal and vertical lines represent the division between Seyfert galaxies and LINERs (low-ionization nuclear emission-line region galaxies) according to Ho et al. (1997). Dots correspond to a subsample of emission line objects, including $H II$ galaxies, from SDSS-DR3, from López (2005). Triangles correspond to $H II$ regions from the sample of Pérez-Montero & Díaz (2005). They have been split into low-metallicity (upside down triangles) and high-metallicity regions (upward triangles) according to the criterion by Díaz & Pérez-Montero (2000) based on oxygen and sulphur abundance parameters.

for the nucleus. Masses derived from the $H\beta$ velocity dispersion under the assumption of a single component for the gas would have been underestimated by factors of between approximately 2 and 4. We have found that only two of the regions, R4 and R5, seem to possess just one knot showing up in the continuum image and coincident with the $H\alpha$ emission. The sizes of these knots are 2.9 and 3.2 pc, respectively. The rest of the regions are made up of several knots which presumably correspond to individual star clusters. Their sizes are between 4.9 and 1.7 pc, at the limit of the resolution. For comparison, the size of cluster A in NGC 1569 is 1.9 pc, as given by Meurer et al. (1995). The sizes and absolute visual magnitudes estimated for each individual star cluster (e.g. $M_v = -12.55$ for R4 derived from the *HST* image) are in the ranges established by Meurer et al. (1995) in the definition of a super star cluster (SSC).

Other estimates of the masses of these regions have been obtained from the fitting of broad-band colours or spectra with the use of stellar population synthesis models. Elmegreen et al. (1997) from near-IR photometry in the *J* and *K* bands and models by Leitherer & Heckman (1995) for instantaneous star formation and solar and twice solar metallicity, derive masses of the CNSFRs from 1 to $10 \times 10^5 M_{\odot}$. Colina et al. (1997) from UV [*International Ultraviolet Explorer (IUE)*] spectra and instantaneous burst models by Mas-Hesse & Kunth (1991) derived a value of $3 \times 10^5 M_{\odot}$ for the whole star-forming ring. In both cases, in fact, these observables

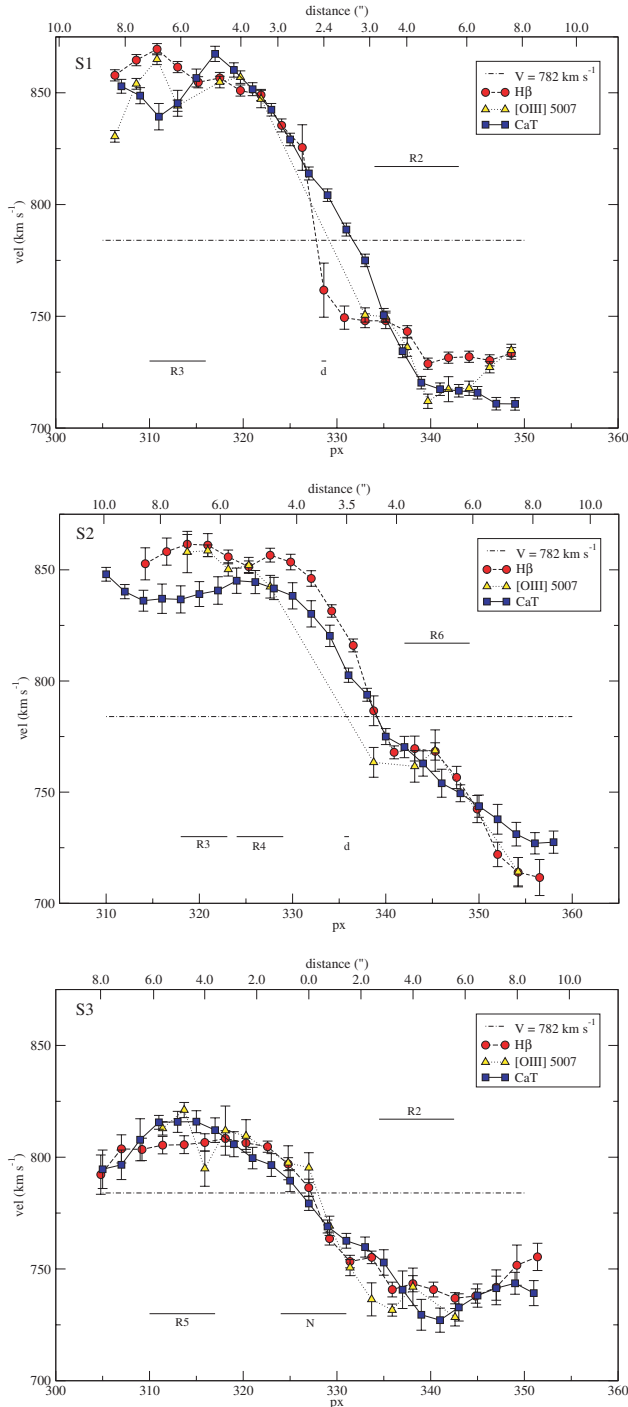


Figure 13. Radial velocities along the slit versus pixel number for each slit position (upper panel: S1; middle panel: S2; lower panel: S3) as derived from the gas emission lines (circles: H β ; triangles: [O III]) and the stellar absorption ones (squares). The individual CNSFRs and the nucleus, ‘N’, or the closest position to it, ‘d’, are marked in the plots. The dashed-dotted line is the systemic velocity of NGC 3351 derived by Planesas et al. (1997). The distance in arcsec from the nucleus is displayed in the upper x-axis of each panel.

trace the young massive population which constitutes only part of the total mass.

The masses derived here for the circumnuclear star-forming individual clusters of NGC 3351 are between 1.8 and $8.7 \times 10^6 M_{\odot}$. These values are between 5.5 and 26 times the mass derived for the

SSC A in NGC 1569 by Ho & Filippenko (1996a) from stellar velocity dispersion measurements using red ($\sim 6000 \text{ \AA}$) spectra, which is $(3.3 \pm 0.5) \times 10^5 M_{\odot}$ and larger than masses derived kinematically for SSC in irregular galaxies (McCradly, Gilbert & Graham 2003; Larsen, Brodie & Hunter 2004). They are also larger than those derived by Benedict et al. (2002) for the individual circumnuclear clusters of NGC 4314 from *HST* imaging data following the procedure of Elmegreen & Salzer (1999), which are in the range $0.2 \times 10^4 \leq M \leq 1.6 \times 10^4 M_{\odot}$. However, also the H β luminosities of the NGC 4314 clusters are lower than those of NGC 3351 by a factor of about 40.

The masses of the ionizing stellar clusters of the CNSFRs, as derived from their H α luminosities, are between 4.1×10^5 and $2.4 \times 10^6 M_{\odot}$ for the star-forming regions, and is $3.1 \times 10^5 M_{\odot}$ for the nucleus (see Table 6). These values are comparable to that derived by González-Delgado et al. (1995) for the circumnuclear region A in NGC 7714 ($5.1 \times 10^5 M_{\odot}$). In column 11 of Table 6 we show a comparison (in percentage) between ionizing stellar masses of the circumnuclear regions and their dynamical masses. These values vary approximately in the range 1–11 per cent for the CNSFRs, and is 0.9 per cent for the nucleus. Since the CaT absorption features are dominated by young stars (see discussion above, Section 3.3), and the M_{ion}/M_* fraction is still remarkably small in the case of the CNSFRs composed of single knots (R4 and R5, for which the dynamical mass is most robustly estimated), we can assume that our upper limits to the dynamical masses, in spite of the limitations of the method used to derive them, are rather tight. Then, our results concerning the M_{ion}/M_* fraction are robust.

Finally, the masses of the ionized gas vary between 3×10^3 and $8.6 \times 10^4 M_{\odot}$ for the CNSFRs, and is $1 \times 10^3 M_{\odot}$ for the nucleus (see Table 6), also comparable to that derived by González-Delgado et al. (1995) for the circumnuclear region A in NGC 7714 ($3 \times 10^5 M_{\odot}$). They make up a small fraction of the total mass of the regions.

Both the masses of the ionizing stellar clusters and the ionized gas have been derived from the H α luminosity of the CNSFRs assumed to consist of one single component. However, if we consider only the broad component whose kinematics follows that of the stars in the regions, all derived quantities would be smaller by a factor of 2.

5 SUMMARY AND CONCLUSIONS

We have measured gas and stellar velocity dispersions in five CNSFRs and the nucleus of the barred spiral NGC 3351. The stellar dispersions have been measured from high-resolution spectra of the CaT lines at $\lambda\lambda 8494, 8542, 8662 \text{ \AA}$, while the gas velocity dispersions have been measured by Gaussian fits to the H β $\lambda 4861 \text{ \AA}$ line on high dispersion spectra.

Stellar velocity dispersions are between 39 and 67 km s^{-1} , about 20 km s^{-1} larger than those measured for the gas. However, the best Gaussian fits involved two different components for the gas: a ‘broad component’ with a velocity dispersion similar to that measured for the stars, and a ‘narrow component’ with a dispersion lower than the stellar one by about 30 km s^{-1} .

When plotted in a [O III]/H β versus [N II]/H α diagram, the two systems are clearly segregated with the narrow component having the lowest excitation and being among the lowest excitation line ratios detected within the SDSS data set of starburst systems.

Values for the dynamical masses of the CNSFRs have been derived from stellar velocity dispersions and are in the range between 4.9×10^6 and $4.3 \times 10^7 M_{\odot}$ for the CNSFRs and is $3.5 \times 10^7 M_{\odot}$ for the nuclear region inside the inner 11.3 pc. Masses derived from

the $H\beta$ velocity dispersion under the assumption of a single component for the gas would have been underestimated by factors of between approximately 2 to 4.

The derived masses for the individual clusters of NGC 3351 are between 1.8 and $8.7 \times 10^6 M_\odot$. These values are between 5.5 and 26 times the mass derived for the SSC A in NGC 1569 by Ho & Filippenko (1996a) and larger than other kinematically derived SSC masses.

Masses of the ionizing stellar clusters of the CNSFRs have been derived from their $H\alpha$ luminosities under the assumption that the regions are ionization bound and without taking into account any photon absorption by dust. Their values are between 4.1×10^5 and $2.4 \times 10^6 M_\odot$ for the star-forming regions, and is $3.1 \times 10^5 M_\odot$ for the nucleus (see Table 6), comparable to that derived by González-Delgado et al. (1995) for the circumnuclear region A in NGC 7714. Therefore, the ratio of the ionizing stellar population to the total dynamical mass is between 0.01 and 0.11.

Derived masses for the ionized gas vary between 3×10^3 and $8.6 \times 10^4 M_\odot$ for the CNSFRs, and is $1 \times 10^3 M_\odot$ for the nucleus, also comparable to that derived by González-Delgado et al. (1995).

It is interesting to note that, according to our findings, the SSC in CNSFRs seem to contain composite stellar populations. Although the youngest one dominates the UV light and is responsible for the gas ionization, it constitutes only about 10 per cent of the total. This can explain the low EWs of emission lines measured in these regions. This may well apply to the case of other SSC and therefore conclusions drawn from fits of single stellar population (SSP) models should be taken with caution (e.g. McCrady et al. 2003; Larsen et al. 2004). Furthermore, the composite nature of the CNSFRs means that star formation in the rings is a process that has taken place over time periods much longer than those implied by the properties of the ionized gas.

The rotation velocities derived for both stars and gas are in reasonable agreement, although in some cases the gas shows a velocity slightly different from that of the stars. The rotation curve corresponding to the position going through the centre of the galaxy shows maximum and minimum values at the position of the circumnuclear ring, as observed in other galaxies with CNSFRs. The differences in velocity between gas and stars can be interpreted as motions of the ionized hydrogen deviating from rotation and consistent with a radial infall to the central regions of the galaxy. Our results are consistent with those found by Rubin et al. (1975) and would yield an infall velocity of about 25 km s^{-1} .

The existence of more than one velocity component in the ionized gas corresponding to kinematically distinct systems, deserves further study. Several results derived from the observations of the different emission lines could be affected, among others: the classification of the activity in the central regions of galaxies, the inferences about the nature of the source of ionization, the gas abundance determinations, the number of ionizing photons from a given region and any quantity derived from them, etc. To disentangle the origin of these two components it will be necessary to map these regions with high spectral and spatial resolution and much better S/N ratio in particular for the O^{2+} lines. 3D spectroscopy with IFUs would be the ideal tool to approach this issue.

ACKNOWLEDGMENTS

We are indebted to Jesús López who provided the data on the SDSS sample prior to publication. We acknowledge fruitful discussions with Horacio Dottori, Enrique Pérez, Enrique Pérez-Montero and José Vílchez. We thank very much an anonymous referee for his/her

careful examination of our manuscript. We have found the report extremely thorough and undoubtedly it has helped to improve the contents of this paper.

The WHT is operated in the island of La Palma by the Isaac Newton Group in the Spanish Observatorio del Roque de los Muchachos of the Instituto de Astrofísica de Canarias. We thank the Spanish allocation committee (CAT) for awarding observing time.

Some of the data presented in this paper were obtained from the Multimission Archive at the Space Telescope Science Institute (MAST). Space Telescope Science Institute (STScI) is operated by the Association of Universities for Research in Astronomy, Inc., under NASA contract NAS5-26555. Support for MAST for non-*HST* data is provided by the NASA Office of Space Science via grant NAG5-7584 and by other grants and contracts.

This research has made use of the NASA/IPAC Extragalactic Database (NED) which is operated by the Jet Propulsion Laboratory, California Institute of Technology, under contract with the National Aeronautics and Space Administration.

This research has made use of the SIMBAD data base, operated at CDS, Strasbourg, France.

This work has been supported by DGICYT grant AYA-2004-02860-C03. GFH and MVC acknowledge support from the Spanish MEC through FPU grants AP2003-1821 and AP2004-0977. AID acknowledges support from the Spanish MEC through a sabbatical grant PR2006-0049. Furthermore, partial support from the Comunidad de Madrid under grant S-0505/ESP/000237 (ASTRO-CAM) is acknowledged. Support from the Mexican Research Council (CONACYT) through grant 49942 is acknowledged by ET and RT. We thank the hospitality of the Institute of Astronomy of Cambridge where this paper was written.

REFERENCES

- Alloin D., Nieto J.-L., 1982, *A&AS*, 50, 491
- Baldwin J. A., Phillips M. M., Terlevich R., 1981, *PASP*, 93, 5
- Benedict G. F., Howell D. A., Jørgensen L., Kenney J. D. P., Smith B. J., 2002, *AJ*, 123, 1411
- Binney J., Tremaine S., 1987, *Galactic Dynamics*. Princeton Univ. Press, Princeton, NJ, p. 747
- Castellanos M., Díaz A. I., Terlevich E., 2002, *MNRAS*, 329, 315
- Cid Fernandes R., Heckman T., Schmitt H., Delgado R. M. G., Storchi-Bergmann T., 2001, *ApJ*, 558, 81
- Colina L., García Vargas M. L., Mas-Hesse J. M., Alberdi A., Krabbe A., 1997, *ApJ*, 484, L41
- Colina L., González-Delgado R., Mas-Hesse J. M., Leitherer C., 2002, *ApJ*, 579, 545
- Devereux N. A., Kenney J. D., Young J. S., 1992, *AJ*, 103, 784
- Díaz A. I., 1988, *MNRAS*, 231, 57
- Díaz A. I., 1998, *Ap&SS*, 263, 143
- Díaz A. I. et al., 2000, *MNRAS*, 312, 130
- Díaz A. I., Terlevich E., Terlevich R., 1989, *MNRAS*, 239, 325
- Díaz R., Carranza G., Dottori H., Goldes G., 1999, *ApJ*, 512, 623
- Díaz A. I., Álvarez-Álvarez M., Terlevich E., Terlevich R., Portal M. S., Arétxaga I., 2000, *MNRAS*, 311, 120
- Díaz A. I., Terlevich E., Castellanos M., Hägele G. F., 2006, in Israelian G., Meynet G., eds, *Proc. Metal Rich Universe Conference*. Cambridge Univ. Press, Cambridge, in press (astro-ph/0610787)
- Elmegreen D. M., Salzer J. J., 1999, *AJ*, 117, 764
- Elmegreen D. M., Chromey F. R., Santos M., Marshall D., 1997, *AJ*, 114, 1850
- García-Vargas M. L., Bressan A., Díaz A. I., 1995, *A&AS*, 112, 35
- González-Delgado R. M. et al., 1994, *ApJ*, 437, 239
- González-Delgado R. M., Pérez E., Díaz A. I., García-Vargas M. L., Terlevich E., Vílchez J. M., 1995, *ApJ*, 439, 604

- González-Delgado R. M., Heckman T., Leitherer C., Meurer G., Krolik J., Wilson A. S., Kinney A., Koratkar A., 1998, *ApJ*, 505, 174
- Graham J. A. et al., 1997, *ApJ*, 477, 535
- Hägele G. F., Pérez-Montero E., Díaz A. I., Terlevich E., Terlevich R., 2006, *MNRAS*, 372, 293
- Ho L. C., Filippenko A. V., 1996a, *ApJ*, 466, L83
- Ho L. C., Filippenko A. V., 1996b, *ApJ*, 472, 600
- Ho L. C., Filippenko A. V., Sargent W. L. W., 1997, *ApJS*, 112, 315
- Hoyos C., Díaz A. I., 2006, *MNRAS*, 365, 454
- Jiménez-Benito L., Díaz A. I., Terlevich R., Terlevich E., 2000, *MNRAS*, 317, 907
- Kauffmann G. et al., 2003, *MNRAS*, 346, 1055
- Kewley L. J., Dopita M. A., Sutherland R. S., Heisler C. A., Trevena J., 2001, *ApJ*, 556, 121
- Kurtz M. J., Mink D. J., 1998, *PASP*, 110, 934
- Larsen S. S., Brodie J. P., Hunter D. A., 2004, *AJ*, 128, 2295
- Leitherer C., Heckman T. M., 1995, *ApJS*, 96, 9
- López J., 2005, MSc thesis, INAOE
- Macchetto F., Colina L., Golombek D., Perryman M. A. C., di Serego Alighieri S., 1990, *ApJ*, 356, 389
- McCraday N., Gilbert A. M., Graham J. R., 2003, *ApJ*, 596, 240
- Maoz D., Barth A. J., Sternberg A., Filippenko A. V., Ho L. C., Macchetto F. D., Rix H.-W., Schneider D. P., 1996, *AJ*, 111, 2248
- Mas-Hesse J. M., Kunth D., 1991, *A&AS*, 88, 399
- Melnick J., Terlevich R., Moles M., 1988, *MNRAS*, 235, 297
- Melnick J., Tenorio-Tagle G., Terlevich R., 1999, *MNRAS*, 302, 677
- Meurer G. R., Heckman T. M., Leitherer C., Kinney A., Robert C., Garnett D. R., 1995, *AJ*, 110, 2665
- Miller J. S., Mathews W. G., 1972, *ApJ*, 172, 593
- Nelson C. H., Whittle M., 1995, *ApJS*, 99, 67
- Osterbrock D. E., Fulbright J. P., Martel A. R., Keane M. J., Trager S. C., Basri G., 1996, *PASP*, 108, 277
- Palacios J., García-Vargas M. L., Díaz A., Terlevich R., Terlevich E., 1997, *A&A*, 323, 749
- Pérez-Montero E., Díaz A. I., 2003, *MNRAS*, 346, 105
- Pérez-Montero E., Díaz A. I., 2005, *MNRAS*, 361, 1063
- Pérez-Olea D., 1996, PhD thesis, Universidad Autónoma de Madrid
- Planesas P., Colina L., Pérez-Olea D., 1997, *A&A*, 325, 81
- Prada F., Greve A., McKeith C. D., 1994, *A&A*, 288, 396
- Rubin V. C., Peterson C. J., Ford W. K., Jr, 1975, *ApJ*, 199, 39
- Salpeter E. E., 1955, *ApJ*, 121, 161
- Sandage A., Tammann G. A., 1987, *A Revised Shapley-Ames Catalog of Bright Galaxies*, 2nd edn. Carnegie Institution of Washington Publication, Washington
- Sérsic J. L., Pastoriza M., 1967, *PASP*, 79, 152
- Telesco C. M., Decher R., 1988, *ApJ*, 334, 573
- Terlevich E., Terlevich R., Díaz A. I., Pastoriza M. G., Dottori H., 1990, *MNRAS*, 242, 48p
- Tonry J., Davis M., 1979, *AJ*, 84, 1511

This paper has been typeset from a $\text{\TeX}/\text{\LaTeX}$ file prepared by the author.